The Astrophysical Journal, 844:115 (12pp), 2017 August 1 https://doi.org/10.3847/1538-4357/aa7b87

Orbital Elements and Stellar Parameters of the Active Binary UX Arietis

C. A. Hummel[1], J. D. Monnier[2], R. M. Roettenbacher[3], G. Torres[4], G. W. Henry[5], H. Korhonen[6], A. Beasley[7], G. H. Schaefer[8], N. H. Turner[8], T. Ten Brummelaar[8], C. D. Farrington[8], J. Sturmann[8], L. Sturmann[8], F. Baron[9], and S. Kraus[10]
[1] European Southern Observatory, Karl-Schwarzschild-Str. 2, D-85748 Garching, Germany; chummel@eso.org
[2] Department of Astronomy, University of Michigan, Ann Arbor, MI 48109, USA
[3] Department of Astronomy, Stockholm University, SE-106 91 Stockholm, Sweden
[4] Harvard-Smithsonian Center for Astrophysics, 60 Garden Street, Cambridge, MA 02138, USA
[5] Center of Excellence in Information Systems, Tennessee State University, Nashville, TN 37209, USA
[6] Dark Cosmology Centre, Niels Bohr Institute, University of Copenhagen, Juliane Maries Vej 30, DK-2100 Copenhagen, Denmark
[7] National Radio Astronomy Observatory, 520 Edgemont Road, Charlottesville, VA 22902, USA
[8] The CHARA Array of Georgia State University, Mount Wilson Observatory, Mount Wilson, CA 91203, USA
[9] Department of Physics and Astronomy, Georgia State University, Atlanta, GA, USA
[10] School of Physics, Astrophysics Group, University of Exeter, Stocker Road, Exeter EX4 4QL, UK
Received 2017 May 22; revised 2017 June 20; accepted 2017 June 22; published 2017 July 28

Abstract

Stellar activity observed as large surface spots, radio flares, or emission lines is often found in binary systems. UX Arietis exhibits these signs of activity, originating on the K0 subgiant primary component. Our aim is to resolve the binary, measure the orbital motion, and provide accurate stellar parameters such as masses and luminosities to aid in the interpretation of the observed phenomena. Using the CHARA six-telescope optical long-baseline array on Mount Wilson, California, we obtained amplitudes and phases of the interferometric visibility on baselines up to 330 m in length, resolving the two components of the binary. We reanalyzed archival Center for Astrophysics spectra to disentangle the binary component spectra and the spectrum of the third component, which was resolved by speckle interferometry. We also obtained new spectra with the Nordic Optical Telescope, and we present new photometric data that we use to model stellar surface spot locations. Both interferometric visibilities and spectroscopic radial velocities are modeled with a spotted primary stellar surface using the Wilson–Devinney code. We fit the orbital elements to the apparent orbit and radial velocity data to derive the distance (52.1 ± 0.8 pc) and stellar masses ($M_P = 1.30 \pm 0.06\ M_\odot$, $M_S = 1.14 \pm 0.06\ M_\odot$). The radius of the primary can be determined to be $R_P = 5.6 \pm 0.1\ R_\odot$ and that of the secondary to be $R_S = 1.6 \pm 0.2\ R_\odot$. The equivalent spot coverage of the primary component was found to be 62% with an effective temperature 20% below that of the unspotted surface.

Key words: binaries: spectroscopic – stars: activity – stars: individual (UX Ari) – stars: late-type – starspots

1. Introduction

Stars in close binaries are subject to increased magnetic activity and hence evolution that can be very different from that of single stars. Apart from mass transfer in single- or double-contact binaries, a companion's tidal interaction can spin up slowly rotating late-type stars, which may produce starspots due to increased magnetic field strengths.

Such phenomena may be observed on the primary components of the class of RS Canum Venaticorum (RS CVn) binaries in which an evolved late-type star is orbited by a less-evolved star, often still on the main sequence (Hall 1976; Montesinos et al. 1988). Signs of activity also include flares, enhanced Ca II H and K emission, and radio/X-ray emission. Radio emission of active stars is caused by the gyrosynchrotron process in plasma contained by the large-scale magnetic field loops (Franciosini & Chiuderi Drago 1995) in the coronae of these stars. The geometry and extent of the magnetospheres in magnetically active stars control stellar winds and therefore the angular momentum evolution in binary systems.

UX Arietis (UX Ari, HD 21242, HIP 16042) is now known as one of the most active members of the RS CVn binaries following its discovery based on strong H and K emission by Popper (1956) and classification as a double-lined spectroscopic binary (component A) with a subgiant primary component (Aa) of type K0 and a main-sequence companion (Ab) of type G5 by Carlos & Popper (1971). Doppler imaging based on high-resolution spectroscopy has revealed a number of high- and low-latitude spots on the surface of the subgiant primary of UX Ari (Vogt et al. 1991; Aarum et al. 1999; Gu et al. 2004, 2005). Vogt et al. (1991) also concluded that the angular velocity of the equator of this component is synchronized with the orbital angular velocity. Elias et al. (1995) modeled the light curve of UX Ari using a small number of spots and established a correlation between the flaring radio emission and the starspot distribution on the surface of the primary of UX Ari between 1992 and 1993 using observations from the Very Large Array (VLA) and visual photometry. They concluded that the flares were located close to the starspot groups. Just a couple years later, the brightest flare ever in such stars (up to this event) was observed in the ultraviolet region (Henry & Hall 1997), as well as in the radio (A. Beasley et al., in preparation).

The systemic radial velocity (RV) of UX Ari was found to change slowly over several years and then more rapidly, by 4 km s^{-1}, between 1996 and 2000 (Duemmler & Aarum 2001). The lines of a third star (component B) of type G5V could be seen in the combined spectrum by Aarum Ulvås & Engvold (2003b), but the star was not considered to be part of the UX Ari system despite the fact that it had been known since 1985 from speckle observations by McAlister et al. (1987) and had decreased its separation from 0.″4 to less that 0.″1 about 15 yr later.

Detailed modeling of the radio sources for past and future epochs requires an unambiguous knowledge of the stellar

Table 1
Calibrator Information for Interferometric Observations

Star	Distance (deg)	Diameter (mas)	Error (mas)
HR 1921	58.3	0.709[a]	0.049
γ Tri	81.3	0.470[a]	0.033
θ Gem	17.1	0.813[a]	0.056
ζ Per	69.6	0.530[b]	0.030

Notes.
[a] Bonneau et al. (2006).
[b] Challouf et al. (2014) with larger errors.

positions in the system with submilliarcsecond accuracy. With orbital periods between a few days and a few weeks, RS CVn stars are resolved only by optical interferometry (or in the radio by Very Long Baseline Interferometry). To this end, we obtained observations with the Center for High Angular Resolution Astronomy (CHARA) interferometer and were able to resolve the 1.7 mas semimajor axis of the 6.4 day orbit. We analyzed the orbital motion of UX Ari and combined our results with a reanalysis of spectroscopic material obtained originally by Massarotti et al. (2008), along with other published RVs, to determine the distance to UX Ari and the fundamental stellar parameters of its components. Finally, we were able to image a single large starspot on the surface of the subgiant primary.

2. Observations and Data Reduction

2.1. Interferometry

Observations were carried out during nine nights in 2012 November and December using the Michigan InfraRed Combiner (MIRC; Monnier et al. 2004) attached to Georgia State University's CHARA array (ten Brummelaar et al. 2005). The observation dates are listed in Table 4 (column 1). In most nights, the *H*-band light of all six telescopes was combined, allowing the measurement of the visibility amplitude on all 15 baselines between the telescopes and closure phases on 10 triple-baseline combinations of three stations. The interferometric point-spread function (PSF) was typically 0.7 mas in diameter. The data were reduced and calibrated with the standard MIRC pipeline (Monnier et al. 2007, 2012; Zhao et al. 2009; Che et al. 2011). The stars used to calibrate the data are given in Table 1. In Figure 1, we show the (squared) visibility amplitude as a function of baseline length. The significant range of values already indicates that at least one component diameter is resolved.

2.2. Spectroscopy

2.2.1. Previously Published Observations

We include RVs published by Carlos & Popper (1971; data set C&P) and Duemmler & Aarum (2001; data set KP/McD). The former were obtained from observations between 1954 and 1970 at the Mt. Wilson and Lick observatories, the latter from observations between 1999 and 2000 at the McDonald and Kitt Peak observatories. The corresponding electronic data were downloaded from the SB9 database.[11]

[11] http://sb9.astro.ulb.ac.be/DisplayFull.cgi?169+2

2.2.2. CfA Observations

The high-resolution spectra of UX Ari used in this work were originally obtained by Massarotti et al. (2008) at the Harvard-Smithsonian Center for Astrophysics (CfA) between 2003 December and 2005 February. They were gathered with an echelle spectrograph mounted at the Cassegrain focus of the 1.5 m Wyeth reflector at the Oak Ridge Observatory, situated in the town of Harvard, Massachusetts. The resolving power of this instrument is $R \approx 35{,}000$. A single order spanning 45 Å was recorded with an intensified photon-counting Reticon detector at a central wavelength of about 5187 Å that includes the Mg I triplet. The signal-to-noise ratios of the 17 observations range from 40 to 62 per resolution element of 8.5 km s^{-1}. Massarotti et al. (2008) reported RV measurements for the primary and secondary components of UX Ari and published a double-lined spectroscopic orbital solution. Here we reanalyze these same spectra to extract other information, as well as the velocities of the tertiary component. Our new velocity measurements supersede those of Massarotti et al. (2008).

2.2.3. NOT Observations

New spectroscopic observations of the UX Ari system were obtained with the FIbre-fed Echelle Spectrograph (FIES) high-resolution spectrograph (Telting et al. 2014) at the Nordic Optical Telescope (NOT). The observations were carried out on nine epochs between 2016 November 23 and 2017 January 24. The observations were originally intended for stellar surface mapping with the Doppler imaging technique, so they are well distributed over the orbital phases. FIES has a fixed spectral format giving a wavelength range of 3700–7300 Å in a single exposure. In the current work, the 1.″3 fiber with a resolving power ($\lambda/\Delta\lambda$) of 46,000 was used. The exposure time of 500 s resulted in signal-to-noise ratios at 6300 Å of 150–700 per resolution element, with typical values around 300. Standard calibrations of biases, flat fields, and thorium-argon wavelength calibration frames were obtained during the day before the observing night. All the spectra were reduced with the dedicated FIES reduction software FIEStool.

2.3. Photometry

UX Ari has been monitored each year since 1987 with the Tennessee State University T3 0.4 m Automatic Photometric Telescope (APT) at Fairborn Observatory in southern Arizona. Earlier results from the interval 1987 to 2002 were published by Aarum Ulvås & Henry (2003). Their paper describes the acquisition, reduction, and analysis of the APT data. The light curves obtained in the *B* and *V* passbands provide important constraints for modeling the visibility and RV measurements.

The light curves change slowly on a timescale of ≈1.5 yr (two observing seasons). This can be seen by plotting long-term APT photometry from Aarum Ulvås & Henry (2003) and the newer APT data acquired for this paper by G. Henry in intervals containing two consecutive observing seasons as a function of orbital phase (see Figure 2). The phase curves appear primarily as single, coherent strands despite the fact that the 1.5 yr time intervals contained in each phase plot represent approximately 80 rotation (orbital) cycles. This applies in particular to the interval from 2011 December to 2013 April that includes the MIRC epochs during which no simultaneous observations could be secured.

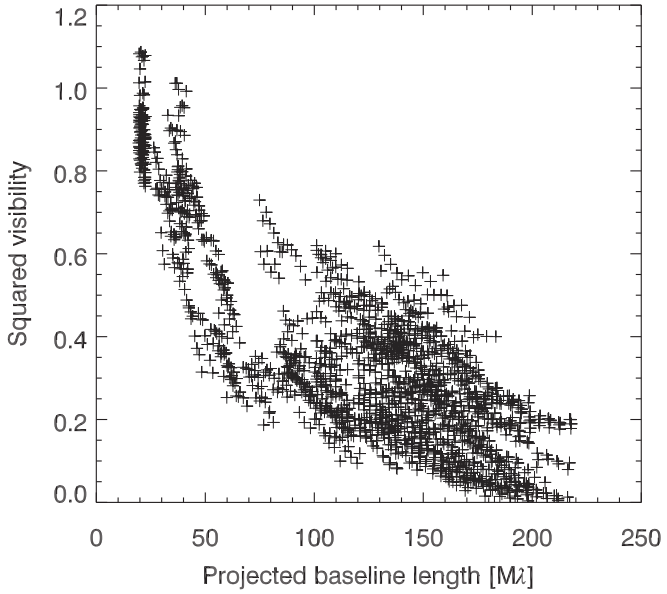

Figure 1. Squared visibilities vs. baseline length in units of Mλ for all nights combined.

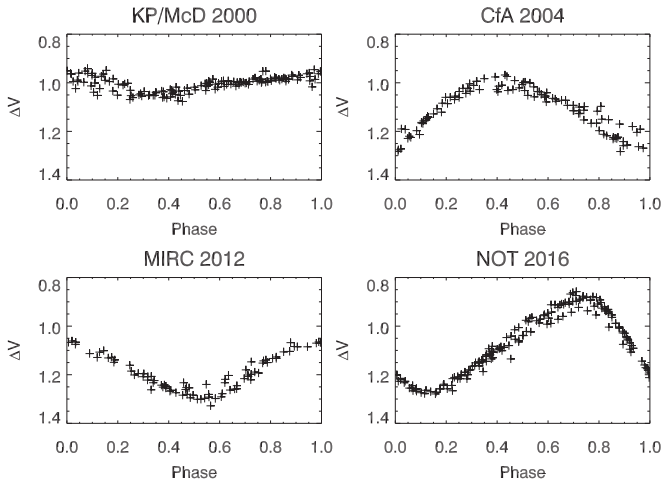

Figure 2. Differential *V*-band light curves acquired with the T3 0.4 m APT as a function of phase based on an orbital period of 6.43787 days for selected intervals of approximately 1 yr (two observing seasons) containing the three spectroscopic data sets (KP/McD 2000, CfA 2004, and NOT 2016) discussed in the text and the interferometric observations (MIRC 2012).

We define zero phase to be when the secondary (less massive) star is at inferior conjunction in front of the primary (more massive) star. Our new ephemeris for zero phase determined in this paper is HJD $= 2,456,238.134 + 6.437888P$, where P is the (unwrapped) phase. This definition of the phase is opposite to the one used by Carlos & Popper (1971) and Elias et al. (1995), which was based on the usual assignment of the cooler component as the secondary.

3. Data Analysis

The extraction of physical component parameters and orbital elements from the visibility data is not a one-step process but requires iterative adjustment of groups of parameters that are correlated to some degree. In Section 3.1, we discuss our imaging of the stars, as this process is model-independent and gave us a first idea about the presence of spots. We then model in Section 3.2 the visibility data with a primary component featuring a single spot and derive high-precision orbital elements of the apparent orbit. In Section 3.3.1, we reanalyze the CfA observations of UX Ari to extract the spectra of all three components to determine their physical parameters and to extract the RVs of the tertiary. We combine the astrometry and radial velocimetry in Section 3.4 to determine the orbital parallax and the stellar masses for the binary component Aa–Ab.

3.1. Imaging and Stellar Surface Modeling

Images were made from each of the nine MIRC data sets using the Markov Chain Imager (MACIM) program (Ireland et al. 2006) with two circular flat priors to include only stellar emission inside the respective stellar radii. The images are shown in Figure 3 and display prominent spot activity on the resolved primary component. At similar orbital phases of the clearly visible secondary component, e.g., on November 24 and December 7 or on November 25 and December 8, a single large spot appears in the same place, indicative of one (or more) spots not moving in the corotating reference frame of the binary. Performing aperture photometry with DS9 (SAOImage) of the images presented here, we found an average H-band magnitude difference of $\Delta H = 1.81 \pm 0.14$. It is obvious that any high-accuracy orbital modeling has to take this fact into account, as otherwise there would be systematic errors in determining the true center-of-mass position of the primary.

We therefore used the 2015 version of the Wilson–Devinney binary system computer model (Wilson & Devinney 1971; Wilson 1990; Wilson & Van Hamme 2014) and its light-curve (LC) program to compute images of a binary with spots on the surface of the primary. The Fourier transform of the images at the measured spacings in the aperture plane provided the model visibility amplitudes and closure phases that were compared to the observed values using the OYSTER interferometric data modeling code. While the diameter of the primary is well resolved by the baselines available at CHARA (see also Figure 1), the diameter of the secondary is only barely so and has to be constrained by other means as well. This can be achieved by removing the magnitude difference between the stars as an independent model parameter and expressing it instead as a function of the stellar effective temperatures and diameters. These parameters are indeed required by LC, and, for the stellar atmosphere models, we adopted effective temperatures $T_{\rm eff}$ and surface gravities $\log g$ as found by our analysis of the CfA spectra (Section 3.3.1). Thus, we fit the diameters of the primary of 0.97 ± 0.02 mas and secondary of 0.35 ± 0.02 mas to the visibility data (see Table 2).

We included a single stationary spot (in the reference frame of the binary) to improve the quality of the fit. LC defines the colatitude of a spot as increasing from zero at the "north" pole (defining the $+z$ axis) to 180° at the south pole and the longitude as increasing counterclockwise from the line connecting the star centers (zero longitude) as seen from the $+z$ axis (Elias et al. 1995).

For each epoch of the observations, we computed a grid of models with spot longitudes between 65° and 255°, latitudes between 20° and 160°, angular radii of the spot between 20° and 50°, and a temperature ratio of spot to photosphere between 0.7 and 0.85. The changing relative location of the components due to orbital motion was taken into account using a preliminary set of orbital elements derived from fitting a pair of uniform disks to each night's visibility data. The best

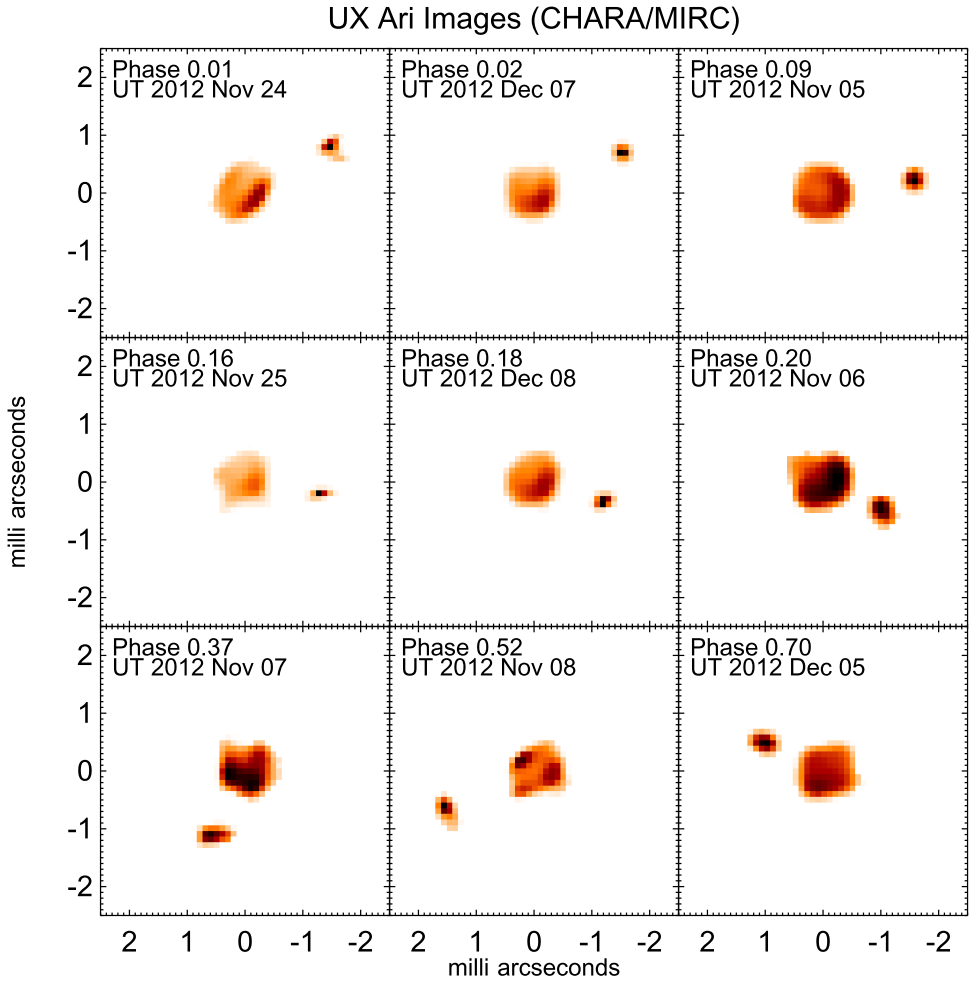

Figure 3. Images of UX Ari (inverted heat color scale: darker colors correspond to brighter regions) obtained from MIRC interferometric data using MACIM. The pixel size is 0.11 mas. East if left, and north is up.

Table 2
LC Specific Parameters of the MIRC Spot Model

Parameter	Aa	Ab
$T_{\rm eff}$[a]	4520 K	5780 K
$\log g$[a]	3.0	4.0
Diameter[b] (mas)	0.97 ± 0.02	0.35 ± 0.02
Limb-darkening coeff.[c]	0.30	0.23
Axial/orb. rotation rate	1	
Gravity darkening exp.[d]	0.1	
Bolometric albedo[d]	0.7	

Notes. Spot parameters are given in Table 3.
[a] See Section 3.3.1.
[b] Limb-darkened.
[c] *H*-band, linear law (van Hamme 1993).
[d] Values for convective envelopes (Lucy 1967; Roettenbacher et al. 2015a).

Table 3
Spot Parameters (All Values in Degrees)

Data Set	Colatitude	Longitude	Radius	$T_{\rm eff}$ Factor
CfA	20	20	45	0.7
MIRC	20	165	45	0.8
NOT	25	300	50	0.7

Figure 4. Model images of the spot at phase zero (left, inferior conjunction of secondary in front of primary) corresponding to maximum light in 2013 and at phase 0.5 (right) corresponding to minimum light in 2012. The color scale is the same as in Figure 3.

agreement with the data was obtained for a spot at a longitude of 165°, latitude 20°, radius 45°, and temperature ratio 0.80. We list the spot parameters for this and other data sets in Table 3. The diameter of the primary is well constrained by the data independently from its assigned effective temperature, while the secondary diameter is much less resolved and represents the value for the *H*-band luminosity that best fits the data given the effective temperature assigned to the secondary. Images of the model for phases zero and 0.5 are shown in Figure 4 and are consistent with the APT photometry (Figure 5), which shows that the maximum light is indeed at phase zero. The final reduced χ^2 of the fit to the visibility data

Table 4
Astrometric Results for the Aa–Ab Component of UX Ari

UT Date	HJD[a] − (2,400,000+)	ρ (mas)	θ (deg)	σ_{maj} (mas)	σ_{min} (mas)	ϕ (deg)	$O-C_\rho$ (mas)	$O-C_\theta$ (deg)
(1)	(2)	(3)	(4)	(5)	(6)	(7)	(8)	(9)
2012 Nov 05	56236.833	1.674	283.48	0.024	0.014	58.1	−0.023	0.18
2012 Nov 06	56237.834	1.086	230.81	0.030	0.013	129.1	−0.000	−0.28
2012 Nov 07	56238.835	1.359	148.65	0.022	0.012	126.4	0.006	0.10
2012 Nov 08	56239.832	1.742	111.00	0.022	0.013	126.3	−0.004	0.43
2012 Nov 24	56255.834	1.763	293.59	0.021	0.013	124.7	0.013	0.03
2012 Nov 25	56256.835	1.300	253.25	0.022	0.013	124.6	0.012	−0.06
2012 Dec 05	56266.835	1.073	48.67	0.025	0.013	120.2	0.002	0.15
2012 Dec 07	56268.833	1.775	290.24	0.023	0.012	124.6	0.033	0.65
2012 Dec 08	56269.834	1.211	244.88	0.019	0.013	122.4	0.010	−0.59

Note.
[a] Astrometric positions given in columns 3 and 4 are for local midnight on the date of observation (HJD for 8 UT).

Table 5
Orbital Elements for Aa–Ab

Parameter	Value
Period (day)	6.437888 ± 0.000007
Semimajor axis (mas)	1.750 ± 0.01
Eccentricity	0 (fixed)
Inclination (deg)	125.0 ± 0.5
Arg. of periastron (primary) (deg)	90 (fixed)
Ascending node (2000.0) (deg)	113.4 ± 0.4
Epoch	HJD 2456238.134 ± 0.002

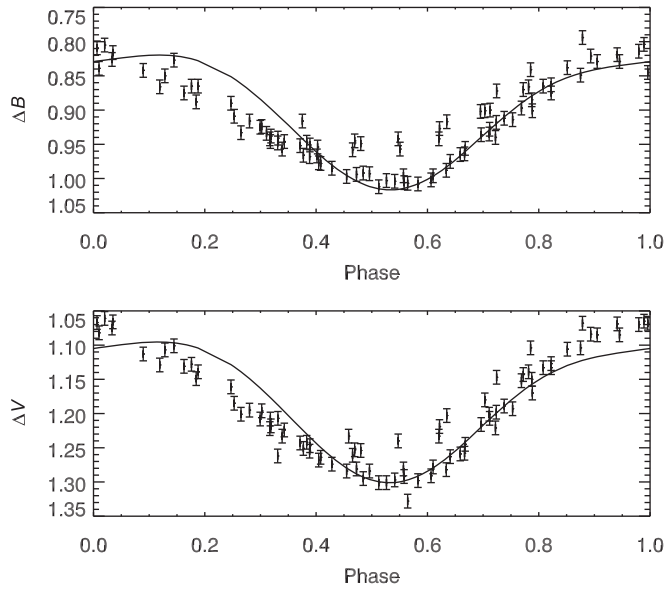

Figure 5. Fit of the 2012 spot model to differential *B*- and *V*-band photometry of UX Ari.

after adjusting the apparent orbit was 1.9 versus $\chi^2 = 3.5$ for an LC model without a spot.

As the flux of the third component expected from its spectral type seems to be not so small (>15% of the total), we computed the expected position of the tertiary for 2012 November from the orbit published by Peterson et al. (2011, Table 4) to be 374 mas from the inner pair. The PSF in the *H* band of a 1 m telescope is about 400 mas, so we expect to see some light coupling into the fibers used by MIRC. The fringe pattern of that light, however, is offset from that of the target itself, so that it only contributes uncorrelated flux. If we add such a component to our model, the fit improves a few percent when the magnitude difference to the primary is 3.5 (i.e., 5% of its flux), while the diameter of the primary decreases by about 2%.

3.2. Apparent Orbit

To derive the relative astrometric positions (ρ, θ) of the secondary with respect to the primary for each night from the visibility data using LC and OYSTER, we chose as fit parameters from the preliminary orbit just the semimajor axis a and position angle of the line of nodes Ω, because separation ρ and position angle θ are not LC model parameters. We then computed the astrometric results for ρ and θ listed in Table 4 (columns 3 and 4) from a and Ω and the other orbital elements. Columns 5 and 6 give the semimajor and semiminor axes of the astrometric uncertainty ellipse, respectively, and column 7 gives the position angle of the major axis.

Both Peterson et al. (2011) and Duemmler & Aarum (2001) published orbital elements of the close pair in UX Ari, the former for the radio centroid of the primary and the latter for the RV curves. Circular orbits were adopted, and we found that our orbit is also consistent with a value of zero for the eccentricity. The final elements of the apparent orbit we fit to the astrometric positions are listed in Table 5, and the orbit is shown in Figure 6. The orbital period was additionally constrained by the RV data (Section 3.4). The uncertainties are based on Gaussian error propagation from the astrometric uncertainty ellipses of Table 4, which were scaled with a common factor to result in a reduced χ^2 of unity for the fit of the orbit to the astrometric data. This procedure has the advantage of equalizing the weights necessary for the combination of the astrometric positions and RVs (see next section) when fitting the orbital parallax and stellar masses, as described in Section 3.4. Our work corrects the inclination found by Duemmler & Aarum (2001), made possible by the absolute phase angle calibration provided by optical interferometry, and corrects the prograde orbit of Peterson et al. (2011) to be retrograde, thanks to our more closely time-spaced observations.

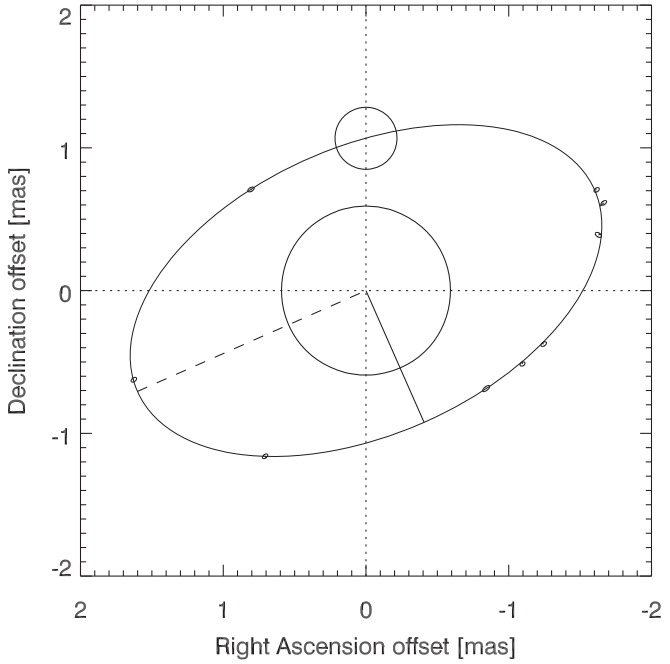

Figure 6. Apparent orbit of Ab around Aa in UX Ari. The circles correspond to stellar diameters in size. The small ellipses are the astrometric positions observed with MIRC and their uncertainties. Since the orbital inclination is larger than 90°, the orbit is retrograde; i.e., the position angle (measured east of north) of the secondary with respect to the primary decreases with time. The dashed line indicates the ascending node. If the secondary is at this position, its RV is positive, i.e., away from the observer, relative to the primary.

3.3. Spectroscopic Analysis

3.3.1. CfA Data

All 17 CfA spectra of UX Ari show lines of three stars. In order to measure the RVs of all components, we used an extension of the two-dimensional cross-correlation algorithm TODCOR (Zucker & Mazeh 1994) to three dimensions (TRICOR; Zucker et al. 1995) with synthetic templates for each component as described by Massarotti et al. (2008). The optimization of the templates is detailed below.

An initial spectroscopic orbital solution for the primary and secondary yielded a secondary velocity semiamplitude of $K_{\rm Ab} = 67.2 \pm 0.2$ km s^{-1} consistent with values obtained by others (e.g., Duemmler & Aarum 2001; Massarotti et al. 2008), but our primary semiamplitude of $K_{\rm Aa} = 63.8 \pm 0.6$ km s^{-1} was significantly larger than previously reported values of 61.5 ± 0.6 km s^{-1} (Massarotti et al. 2008) and 59.4 ± 0.6 km s^{-1} (Duemmler & Aarum 2001). We also noticed a small but significant systematic difference in the velocity zero points of the primary and secondary of 1.4 ± 0.5 km s^{-1}, corresponding to a difference in the center-of-mass velocities, which could be activity-related or due to other reasons such as template mismatch. The tertiary velocities appeared constant with a mean of $\mathrm{RV_B} = +36.79 \pm 0.50$ km s^{-1}. This agrees well with predictions shown in Figure 8 of Peterson et al. (2011) from their solution for the outer orbit of UX Ari.

To check for systematic errors in the velocities, we ran simulations in which we generated artificial triple-lined spectra by combining the same templates used to derive the RVs after shifting them appropriately relative to each other according to our preliminary orbital fit (and a constant velocity of +37 km s^{-1} for the tertiary) and scaling them using the average light ratios described below. We then processed these artificial spectra in the same way as the real spectra and compared the input and output RVs. The differences were applied as corrections to the real RVs and were typically smaller than 2.5 km s^{-1} for the primary, 0.1 km s^{-1} for the secondary, and 2.2 km s^{-1} for the tertiary. These final velocities, including corrections, are listed in Table 6 in the heliocentric frame and have estimated uncertainties of 1.75, 0.50, and 2.0 km s^{-1} for the primary, secondary, and tertiary, respectively. The velocities for the tertiary star from two of our spectra were very poor due to sky contamination and underexposure and are not listed. With the new velocities, the primary/secondary offset disappeared completely, and, while the secondary semiamplitude did not change ($K_{\rm Ab} = 67.2 \pm 0.2$ km s^{-1}), the primary value increased slightly to $K_{\rm Aa} = 64.3 \pm 0.5$ km s^{-1}, making the difference compared to previous determinations more significant. This suggests a real bias in the primary RVs that is probably related to the spottedness of the star.

Table 6
Heliocentric RVs Derived for UX Ari from the CfA Spectra

HJD (2,400,000+)	$\mathrm{RV_{Aa}}$ (km s^{-1})	$\mathrm{RV_{Ab}}$ (km s^{-1})	$\mathrm{RV_B}$ (km s^{-1})
53003.6399	56.60	−13.21	...
53055.5168	73.94	−30.24	37.90
53071.5121	−26.45	70.59	40.10
53078.5412	−45.11	87.93	36.60
53226.8609	−41.40	89.66	35.80
53276.8287	13.92	31.69	36.40
53285.9305	−1.90	48.15	...
53310.6720	−39.09	88.94	39.40
53319.7653	82.13	−40.20	38.20
53329.6398	−42.01	89.05	39.80
53345.6651	84.48	−43.57	37.60
53355.6202	−40.78	89.64	37.30
53370.6594	60.85	−15.35	36.20
53378.6653	77.41	−34.64	36.00
53401.5506	−15.91	63.23	41.10
53413.5187	−40.98	89.86	38.10
53420.5107	−28.79	79.67	36.00

In addition to the velocities, we derived from each spectrum a light ratio between the primary and secondary components ($\ell_{\rm Ab}/\ell_{\rm Aa}$) and between the primary and tertiary ($\ell_{\rm B}/\ell_{\rm Aa}$). The average values are 1.49 ± 0.08 and[12] 0.13 ± 0.02, respectively, at the mean wavelength of our observations (5187 Å). These measurements are displayed as a function of phase in Figure 7. While individual uncertainties are difficult to estimate, the presence of the same pattern of variation in both light ratios suggests that it is real and indicates that it originates in the primary star. We infer that the maximum brightness of the primary occurs around the phase (∼0.5) where it is in front, such that we see its back side. According to this, the darker side of the primary presumably affected by spots would be facing the companion.

Coincidentally, the light curve for the interval 2004 November to 2006 April that is contemporaneous with the CfA spectroscopic observations (Figure 2) also shows a maximum in brightness corresponding to the time when the primary is in front. This motivated us to use the LC code to compute synthetic light curves using a model featuring a spot

[12] We note that Massarotti et al. (2008) reported a value for $\ell_{\rm Ab}/\ell_{\rm Aa}$ that is close to the reciprocal of this and is in error.

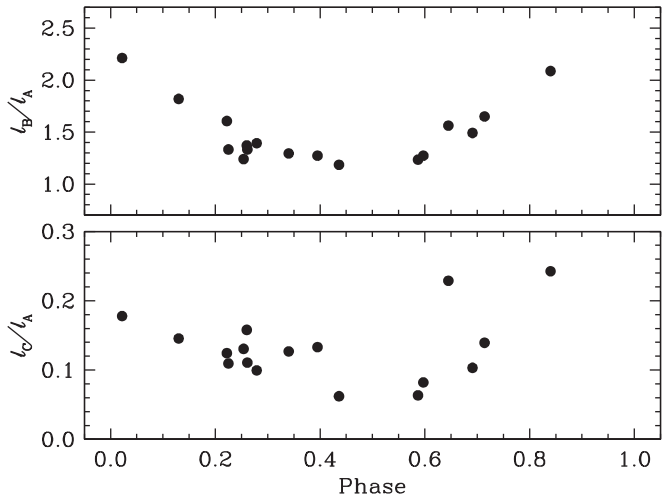

Figure 7. Individual spectroscopic light ratios ℓ_{Ab}/ℓ_{Aa} and $\ell_{B/Aa}$ for UX Ari from the CfA spectra. Phase 0.5 corresponds to inferior conjunction of the primary (subgiant in front).

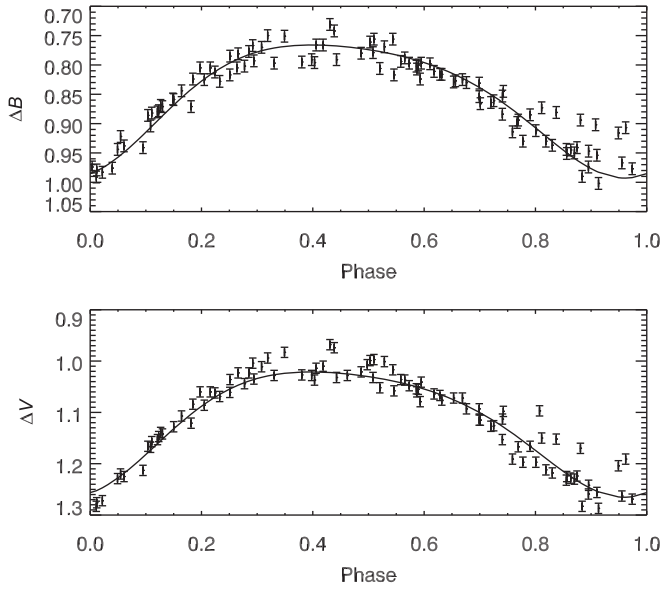

Figure 8. Fit of the 2004 spot model to B and V photometry of UX Ari.

on the primary star facing the secondary (i.e., near a longitude of 0 deg), with the other spot parameters constrained to be similar to those found in Section 3.1. The fit to the APT data of 2004 is shown in Figure 8. We found that the same model also provides a better fit to the RV data, as shown in Figure 9. The LC code computes a flux-weighted average of the RVs associated with each surface element over the entire visible hemisphere (Wilson & Sofia 1976). The RV correction thus corresponds to the wavelength shift between the distorted line's "center" and the line wavelength that goes with the center-of-mass motion. Here "center" means equal areas on the two sides of the midline wavelength (R. E. Wilson 2017, private communication). This definition of the line center used by LC is not necessarily the same as the one corresponding to the specific analysis of the spectra (e.g., profile fitting, cross-correlation, etc.), so some level of systematic error could remain. We found that increasing the spot-related correction to

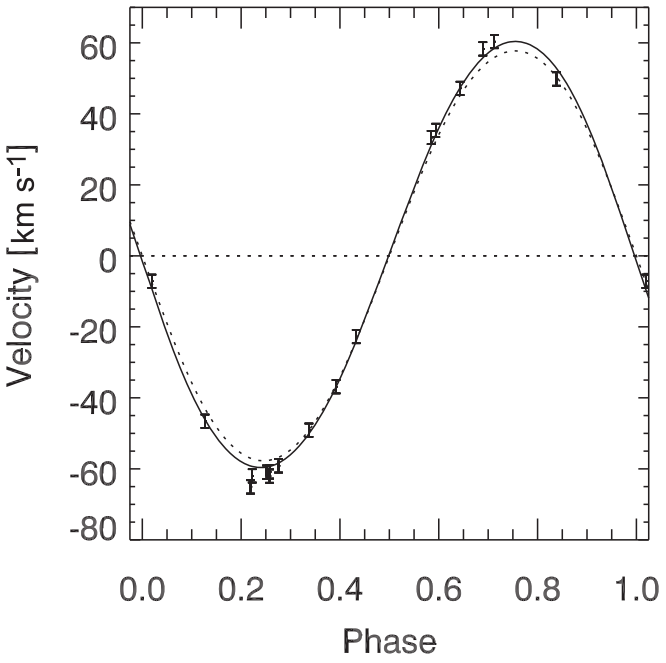

Figure 9. Fit of the CfA RV data for the primary of UX Ari. The dotted line is for a nonspotted surface, while the solid line is for a surface with a single large spot.

the model RVs by 50% would minimize the RV residuals with respect to the orbit.

With the spot-related corrections, the fitted velocity semiamplitude of the primary drops from $K_{Aa} \approx 64$ km s^{-1} to about 60 km s^{-1} (consistent with earlier measurements), while the secondary value remains the same. As spots were generally more prevalent on the primary during the epoch of the CfA observations, the spectroscopic light ratios reported above may not represent the true values for unblemished stars (assuming the secondary and tertiary are not variable), as the primary star could still have been affected even at times of maximum brightness around phase 0.5.

To estimate the effective temperatures and projected rotational velocities of the primary and secondary from the CfA spectra, we ran extensive grids of cross-correlations using TODCOR over wide ranges in $T_{\rm eff}$ and $v \sin i$, ignoring the tertiary given that it is much fainter. We selected the values of the parameters yielding the highest correlation coefficient averaged over all exposures, weighted by the strength of each spectrum. Because of the narrow wavelength range of these observations (only 45 Å), experience has shown that there are strong degeneracies between the temperature, surface gravity $\log g$, and metallicity such that similarly good fits may be obtained by varying those parameters in tandem, although this does not affect the RVs significantly. While Tsuru et al. (1989) reported subsolar metallicity for UX Ari from X-ray spectroscopy, Aarum et al. (1999) had to increase [M/H] by 0.3 to fit the spectral lines used for Doppler imaging. Consequently, we adopted solar metallicity and held $\log g$ fixed at values close to those expected for these stars ($\log g \approx 3.0$ for the primary and $\log g = 4.0$–4.5 for the secondary, on the assumption that it is close to the main sequence). Once the primary and secondary parameters were determined, we held them fixed and ran TRICOR grids to establish the properties of the tertiary. The results for the temperatures are as follows.

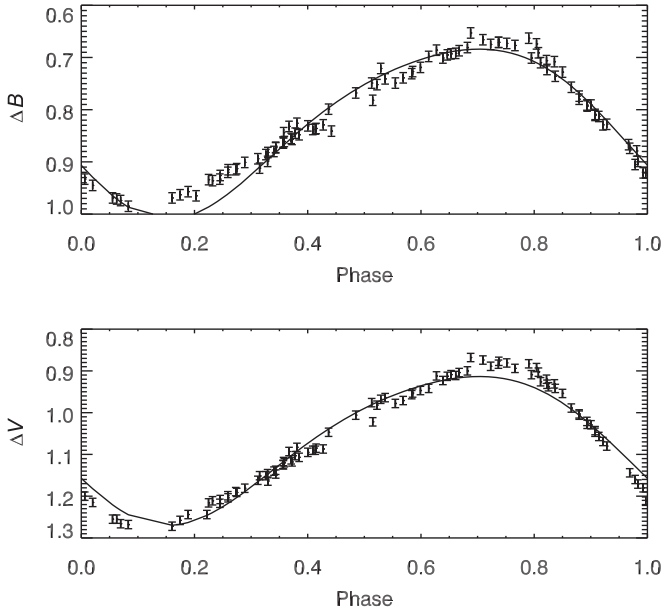

Figure 10. Fit of the 2016 spot model to *B* and *V* photometry of UX Ari.

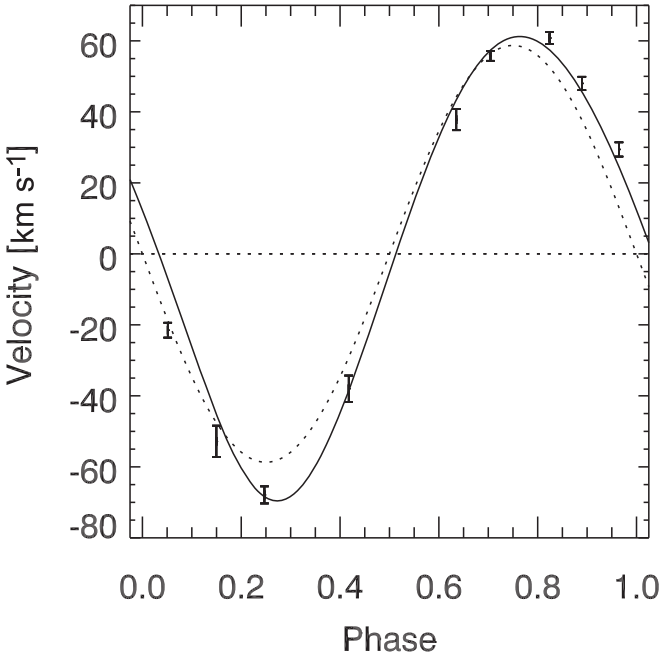

Figure 11. Fit of the NOT RV data for the primary of UX Ari. The dotted line is for a nonspotted surface, while the solid line is for a surface with a single large spot.

Table 7
Heliocentric RVs for UX Ari from the NOT Spectra

HJD (2,400,000+)	RV_{Aa} (km s^{-1})	σ_{Aa} (km s^{-1})	RV_{Ab} (km s^{-1})	σ_{Ab} (km s^{-1})
57758.439	−28.85	4.4	77.36	0.44
57778.379	−43.95	2.4	90.97	0.43
57716.500	61.75	3.0	−26.41	0.77
57721.536	−14.05	3.7	57.43	0.51
57723.382	79.75	1.4	−40.28	0.35
57730.592	84.75	1.7	−36.13	0.55
57731.495	53.35	2.0	10.49	0.83
57737.450	71.95	1.9	−20.01	0.69
57738.492	2.45	2.1	40.23	1.54

1. $T_{\rm eff,Aa} = 4520$ K ($\log g_{\rm Aa} = 3.0$).
2. $T_{\rm eff,Ab} = 5780$ K ($\log g_{\rm Ab} = 4.0$).
3. $T_{\rm eff,Ab} = 6000$ K ($\log g_{\rm Ab} = 4.5$).
4. $T_{\rm eff,B} = 4800$ K ($\log g_{\rm B} = 4.5$).

Estimated temperature uncertainties are 150 K, though this does not account for the unknown metallicity. For example, using a lower metallicity would result in systematically cooler temperatures for all three stars. We caution also that, given the spotted nature of the primary, it is possible that our value for that star might be systematically too low.

The projected rotational velocities we obtain are as follows.

1. $v_{\rm Aa} \sin i = 43 \pm 4$ km s^{-1}.
2. $v_{\rm Ab} \sin i = 8.4 \pm 1.0$ km s^{-1}.
3. $v_{\rm B} \sin i = 4 \pm 3$ km s^{-1}.

Whereas our value for the secondary is similar to other estimates, our value for the subgiant is higher than previously found. Duemmler & Aarum (2001) reported $v_{\rm Aa} \sin i = 39$ km s^{-1}, and Glazunova et al. (2008) measured an even lower value of 34.6 ± 2.1 km s^{-1}. A comparison of values from the latter authors for other stars with independent determinations in the literature may suggest a slight bias toward lower values, but their estimate for the secondary of $v_{\rm Ab} \sin i = 8.3 \pm 0.6$ km s^{-1} is nearly identical to ours, and their tertiary value of $v_{\rm B} \sin i = 6 \pm 1$ km s^{-1} is also consistent with our result. It is not obvious how spots could influence the value for the primary, although we cannot rule out such an effect.

3.3.2. NOT Data

We used the wavelength range 4000–6500 Å for determining the RVs from the FIES observations. This range was divided into 25 subsets with a width of 100 Å each, and the cross-correlation was carried out for each subset independently. This means that for each epoch the final RV measurement is a mean of 25 individual measurements, and the standard deviation of the measurements is used as the error. The accuracy of cross-correlation is increased by improving the sampling of the cross-correlation curve using linear interpolation and fitting a Gaussian to the curve.

The cross-correlation was carried out using a synthetic spectrum as a template. The synthetic spectrum was calculated using the SPECTRUM spectral synthesis code (Gray & Corbally 1994) and Kurucz model atmospheres (Kurucz 1993). The spectrum was matched to the spectral type of the primary of UX Ari, $T = 4500$ K, and $\log g = 3.0$. The line list LUKE. LST (included in the SPECTRUM package), which includes atomic lines and some molecular species, was used in the calculations.

In a few orbital phases, determining the cross-correlation peak for the primary was difficult. This resulted in spurious RV measurements at some wavelength regions. The most deviating values (more than ± 10 km s^{-1} from the median value) were removed when calculating the mean and the error. The RV measurements for the primary used 23–25 subsets at all epochs, except 57738.492, for which only 17 subsets were usable. For the secondary, all 25 subsets were always used. The measured values and their errors for different epochs are given in Table 7.

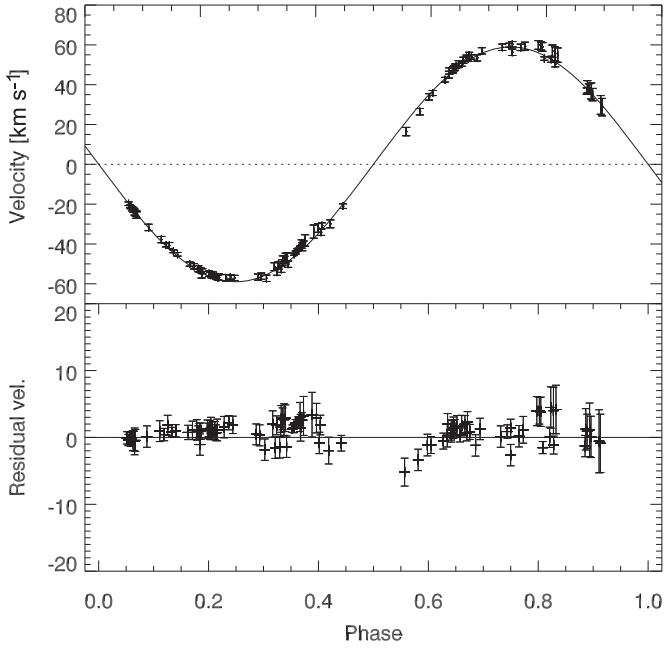

Figure 12. Fit of primary RV data from C&P and KP/McD (CfA and NOT data are shown in Figures 9 and 11, respectively). The systemic velocity of the close pair due to motion around the tertiary was removed. The lower panel shows the residuals. The rms is 1.6 km s^{-1}, and the reduced $\chi^2 = 1.8$.

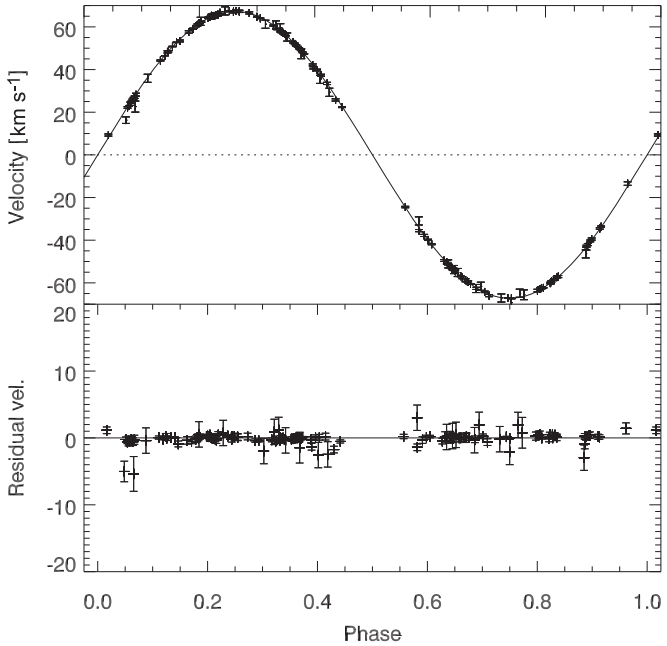

Figure 13. Fit of all secondary RV data of Table 8. The systemic velocity of the close pair due to motion around the tertiary was removed. The lower panel shows the residuals. The rms is 1.0 km s^{-1}, and the reduced $\chi^2 = 1.2$.

As for the CfA data, we fit the pronounced light variations during the observing season including the NOT observations with a single spot at a longitude of 300° (see Table 3). The fit is shown in Figure 10. We found again that the same model also provides a better fit to the RV data, as shown in Figure 11. We point out that the amplitude of the photometric variation is the largest it has been in the last 30 yr, which may be the reason

Table 8
Scaling Factors (f_{Aa}, f_{Ab}) for Uncertainties in RV Data Sets and Fit Results

Data Set	Aa f_{Aa}	Ab f_{Ab}	γ km s^{-1}	K_A km s^{-1}	K_B km s^{-1}
C&P	1.0	1.0	25.5	59.4	66.8
K99	5.6	3.3	25.8	⋯	⋯
M99	1.8	1.5	26.0	⋯	⋯
M00	4.0	1.9	25.8	⋯	⋯
KP/McD	⋯	⋯	25.8	57.7	67.1
CfA04	1.75[a]	0.5[a]	25.5	60.0	67.4
NOT	2.7	1.4	25.6	60.8	66.9

Notes. The γ velocities are already corrected for the motion of the close pair around the tertiary component. Data set KP/McD is the combination of K99, M99, and M00, and CfA04 is our reanalysis of the CfA data.
[a] km s^{-1}.

Table 9
Orbital Parallax and Stellar Parameters

Parameter	Aa	Ab	B
π(mas)	19.20 ± 0.28		
Mass ($M_\odot$)	1.30 ± 0.06	1.14 ± 0.06	0.75[a]
Radius[a] ($R_\odot$)	5.6 ± 0.1	1.6 ± 0.2	0.8 ± 0.1
T_{eff}[b] (K)	4560 ± 100	5670 ± 100	4930 ± 100
Luminosity[b] ($L_\odot$)	9.3 ± 0.7	2.34 ± 0.28	0.38 ± 0.08
log g[c] (cm s^{-2})	3.06 ± 0.04	4.09 ± 0.16	4.51 ± 0.13

Notes.
[a] Peterson et al. (2011).
[b] From photometric model; see Section 4.2.
[c] Derived from mass and radius.

that the single-spot model does not provide a perfect fit despite increasing the spot-related correction to the model RVs by 30% (see also Section 3.3.1).

3.4. Orbital Parallax and Stellar Masses

To determine the stellar masses and orbital parallax, we fit these to the combination of astrometric positions (Table 4) and RVs (Tables 6 and 7). For the latter, we also considered the following RVs published by Carlos & Popper (1971) and (Duemmler & Aarum 2001, data sets K99, M99, and M00 of Table 1). Photometry is not available for the oldest data set, and we therefore could not include corrections for spot activity. Because the photometric variability during 1999 and 2000 (Figure 2) was significantly smaller than that during the CfA and NOT observations, spot activity likely occurred in the same latitude band, in which case there would be no effect on the RVs. Therefore, we did not include spots in our model for the K99, M99, and M00 data sets. As these data contributed the largest number of measurements, they also dominated the fit results. The RV curves for the primary and secondary are shown in Figures 12 and 13, respectively. To investigate the mutual consistency of the spectroscopic data sets, we fit γ and $K_{A,B}$ separately, accounting for changes in the systemic velocity due the motion of the tertiary, for which we adopted a mass of 0.75$M_\odot$ (Peterson et al. 2011). The individual fits also allowed us to determine normalization factors for the reduced χ^2 for the RV uncertainties to achieve a good relative weighting of the data in the final fit, including the astrometric data. The results are given in Table 8. The mean of 25.83 ± 0.17 km s^{-1} for the systemic velocities shows that the

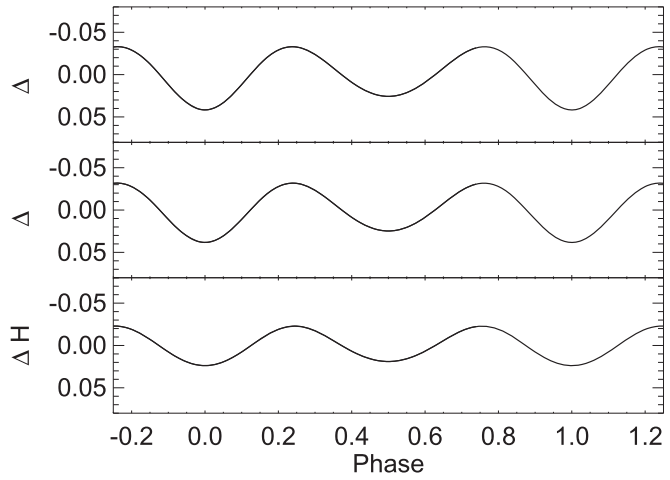

Figure 14. Ellipsoidal light variations predicted by ELC (see the text) using the parameters of UX Ari.

Table 10
Photometry for UX Ari

Component	Band	Measured Magnitude/ Magnitude Difference	Model
AB	*B*	7.31 ± 0.05[a]	7.30
AB	*V*	6.42 ± 0.05[a]	6.43
AB	*H*	3.95 ± 0.1[b]	3.92
AB	*K*	3.83 ± 0.1[b]	3.81
Ab–Aa	5187 Å	0.00 ± 0.2[c]	0.43
Ab–Aa	*V*	0.67 ± 0.2[a]	0.75
Ab–Aa	*H*	1.84 ± 0.14[c]	1.84
B–Ab	*R*	1.90 ± 0.1[a]	2.02
B–A	Hp	3.15 ± 0.20[d]	3.26
B–A	*V*	3.06 ± 0.20[e]	3.24
B–A	*H*	3.4 ± 0.40[c]	3.6

Notes. Combined magnitudes for the triple system are listed in the top half of the table, and magnitude differences are listed in the lower part.
[a] Aarum Ulvås & Engvold (2003a).
[b] Ducati (2002).
[c] This paper.
[d] ESA (1997).
[e] Horch et al. (2012).

motion of the binary around the center of mass with the tertiary is very well corrected.

The stellar parameters and their uncertainties are given in Table 9. We compute the orbital parallax value as 19.20 ± 0.28 mas, in good agreement with the *Hipparcos* parallax of 19.37 ± 0.70 mas (van Leeuwen 2007). We added (in quadrature) to the statistical mass uncertainty (0.03) an estimate of the systematic uncertainty (0.05) based on the remaining difference in the K_A amplitude fitted to all data and to the highest-quality CfA data (see Section 3.3.1).

The tertiary orbit fit by Peterson et al. (2011) to the RV data of Duemmler & Aarum (2001), Massarotti et al. (2008), and Glazunova et al. (2008) and astrometry from the Washington Double Star Catalog is still valid, and the derived orbital parallax (18.9 mas) is consistent with the close pair parallax we derived. The mass of the tertiary according to Peterson et al. (2011) is also given in Table 9.

4. Discussion

4.1. Ellipsoidal Variations

RS CVn primaries (partially) filling their Roche lobes show ellipsoidal light variations as a result, as shown for σ Gem (Roettenbacher et al. 2015b) and o Dra (Roettenbacher et al. 2015a). The size of the primary of UX Ari is only 70% of its Roche lobe, and we therefore do not expect significant ellipsoidal variations. This is shown in Figure 14, which predicts a variation of less than 0.05 mag in the *B*, *V*, and *H* bands based on computations using the software package Eclipsing Light Curve (ELC; Orosz & Hauschildt 2000).

4.2. Photometry

In Table 10, we compile the combined magnitudes and magnitude differences between the components of UX Ari. The combined *B* and *V* values are from Aarum Ulvås & Henry (2003) for the brightest, i.e., least spotted, state of the primary. The combined *H* and *K* values are average magnitudes taken from Ducati (2002). The magnitude differences between the primary and secondary derived from our CfA spectra and the *H*-band MIRC data were taken at maximum brightness of the primary (phases 0.5 and zero, respectively). The difference between tertiary and secondary (both likely not to have spots) was taken from Aarum Ulvås & Engvold (2003a), and the average differences measured between the tertiary and the close pair were derived from speckle interferometry (references in Table 10). The uncertainties of the mean ratios were increased if the photometry included the spotted primary and were average measurements.

We computed a grid of model values based on the NextGen model atmospheres (Hauschildt et al. 1999) for primary effective temperatures $T_{\rm eff}$ in the interval 4000 K $< T_{\rm eff} <$ 4800 K and with a radius $R_{\rm P} = 5.4\ R_\odot$, secondary $T_{\rm eff}$ in the interval 5700 K $< T_{\rm eff} <$ 6000 K and radii of 15%–25% that of the primary, and tertiary $T_{\rm eff}$ in the interval 4600 K $< T_{\rm eff} <$ 4900 K and radii of 11%–15% that of the primary. The diameter of the primary was fixed at the value resulting from the fitted angular diameter (Table 2) and the orbital parallax (Table 9). For the spot temperature, we evaluated values of 70%–90% of that of the unspotted photosphere and a wide range of ratios of area between the spotted and unspotted surface. Using an average spot coverage of 62% of the visible hemisphere with a temperature ratio of 70%, consistent with the angular diameter of the spot used to model the interferometric data (90°), we fit a primary $T_{\rm eff} = 4560$ K (K2IV), secondary radius of $R = 1.5\ R_\odot$ and $T_{\rm eff} = 5670$ K (G4V), and tertiary radius of $R = 0.8\ R_\odot$ and $T_{\rm eff} = 4930$ K (K3V). The data of Table 10 only constrain the diameter ratios; therefore, the diameters of the secondary and tertiary components given here are for a radius of the primary, $R = 5.4\ R_\odot$, as known from the angular diameter fitted to the visibility data combined with the orbital parallax. The radius of the secondary component is not well resolved by the interferometric observations. This is also the reason for the small difference between the angular diameter of the secondary fit to the visibility data by LC (0.35 mas) and the value derived with the photometric model (0.28 mas).

With the exception of the blue magnitude difference at 5187 Å, the photometry is well reproduced by the model (see Table 10). To reproduce the blue magnitude difference of zero at the maximum light of the primary (phase zero; see Figure 7), an earlier secondary type (G0V) would be required, but the agreement with the other photometry would degrade

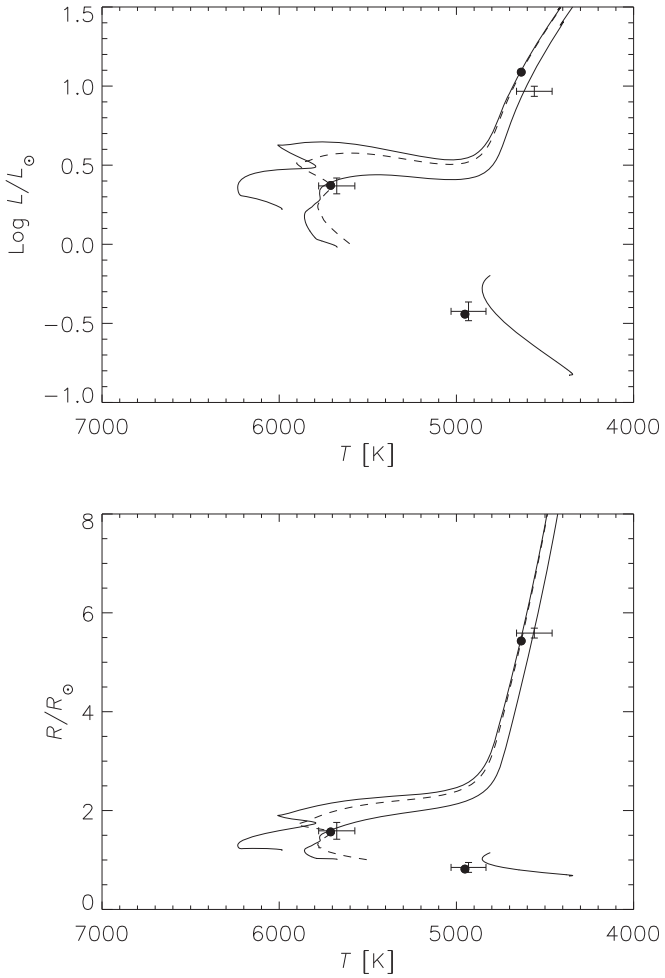

Figure 15. Location of the close components of UX Ari with respect to tracks computed by Choi et al. (2016) showing luminosity (top) and radius (bottom) vs. effective temperature. The dashed line is the best-fit isochrone with an age of 5.6 Gyr.

noticeably. Duemmler & Aarum (2001) hinted at the possibility of the secondary being of an earlier spectral type than originally assigned (G5V) by Carlos & Popper (1971) due to the unexpectedly larger diameter. As we will see in the following, the larger diameter is related to evolution within the main sequence. As the assumption of an earlier type for the secondary would still be inconsistent with the blue magnitude differences at phases when the spot is visible, a better explanation for our observations could be the effect of faculae proposed by Aarum Ulvås & Engvold (2003b) to explain "why UX Ari gets bluer as it gets darker." The faculae surround the spots, and, at phases near zero when the spot was visible in 2004, the blue light was enhanced, as shown in Figure 7.

We used the photometric model to decompose the observed combined magnitudes into component magnitudes, which we converted to absolute magnitudes using the orbital parallax and bolometric corrections tabulated as a function of $(B-V)$ by Flower (1996) and Torres (2010). Since the luminosities thus derived do not depend on the absolute values of the stellar radii (only the ratios are constrained), we found that a match between them and the values consistent with the law of Stefan–Boltzmann would require increasing the measured primary diameter by 3% (1.5σ) to $R = 5.6\ R_\odot$. In Table 9, we list the (absolute) stellar radii and luminosities derived with this photometric model.

The luminosity of the primary was computed as the sum of two hemispheres, one of which corresponds to the unspotted surface (38% of the total) at 4560 K and another that corresponds (62% of the total) to a surface 30% cooler, taking into account the different bolometric corrections.

4.3. Stellar Parameters and Hertzsprung-Russell Diagram

We find that the angular diameters (primary, 0.96 ± 0.08 mas; secondary, 0.23 ± 0.03 mas) computed from the $v \sin i$ values of Glazunova et al. (2008) combined with our orbital inclination, period, and parallax are consistent with the measured values indicating synchronous rotation based on the assumption that the stellar rotation axes are orthogonal to the orbital plane. A subsynchronous rotation rate at 80% would be derived with our reanalyzed CfA value for $v \sin i$, but the difference is only marginally significant, given the measurement uncertainties.

In Figure 15, we show the locations of all three components of UX Ari in the $R - T_{\rm eff}$ and $L - T_{\rm eff}$ diagrams, based on a recent set of models made available by Choi et al. (2016) through a web tool that allows interpolation of tracks for specific masses and metallicities. A good fit can be found for stars with a metallicity $[{\rm Fe/H}] = +0.3$ at an age of 5.6 Gyr, with masses of 1.29, 1.21, and 0.86 $M_\odot$ for the components Aa, Ab, and B, respectively, of UX Ari. The primary component appears slightly cooler and underluminous for its measured mass of 1.30 $M_\odot$, as the stellar model matching its radius has a luminosity 38% larger and is 60 K hotter. The effect of spots on the stellar evolution of low-mass faster-rotating stars has been shown to lead to increased diameters and cooler atmospheres (see Torres et al. 2010), while a similar impact on pre-main-sequence evolution has been shown by Somers & Pinsonneault (2015). The primary of UX Ari thus appears to match the properties of the so-called sub-subgiant (Geller et al. 2017) stars that have been linked to the effect (among others) of magnetic fields (Leiner et al. 2017).

5. Conclusions

Imaging the active binary UX Ari based on interferometric observations resolved the spotted surface of the primary subgiant component. Just a single large spot at high latitudes was required to achieve a good fit to the visibility data and allowed us to derive high-precision elements of the apparent orbit. The spot longitude in the corotating frame was constant during the observations over a time span of at least one month. New and previously published photometry with the APT shows that the spot moves slowly in the corotating frame of the binary but can also disintegrate into several spots. We reanalyzed CfA spectra taken in 2004 and derived RVs from new spectra taken with the NOT in 2016. APT photometry showed the presence of a single spot for these observing seasons, and we applied corrections to the velocities to derive the masses of the stellar components as well as the distance to UX Ari.

UX Ari is an active star, and radio observations have resolved two compact components on more than one occasion. The orbit can now be used to reconstruct the relative stellar

positions at the epochs of the radio observations, which will allow conclusions to be drawn on the emission mechanism.

We thank Robert Wilson (University of Florida) for providing a custom version of his code to compute images of spotted stellar surfaces and for his help with using it. This work is based upon observations obtained with the Georgia State University (GSU) Center for High Angular Resolution Astronomy (CHARA) array at Mount Wilson Observatory. The CHARA array is supported by the National Science Foundation under grant numbers AST-1211929 and AST-1411654. Institutional support has been provided by the GSU College of Arts and Sciences and the GSU Office of the Vice President for Research and Economic Development. The MIRC instrument at the CHARA array was funded by the University of Michigan. F.B., R.R., and J.D.M. acknowledge support from NSF-AST 1210972 and 1108963. G.T. acknowledges partial support from NSF grant AST-1509375. S.K. acknowledges support from an STFC Rutherford Fellowship (ST/J004030/1) and ERC Starting Grant (grant agreement no. 639889). This work is also based on observations made with the Nordic Optical Telescope (NOT), operated by the Nordic Optical Telescope Scientific Association at the Observatorio del Roque de los Muchachos, La Palma, Spain, of the Instituto de Astrofisica de Canarias. This research has made use of the SIMBAD database, operated at the CDS, Strasbourg, France. This research has made use of the Jean-Marie Mariotti Center `SearchCal` service[13] codeveloped by FIZEAU and LAOG/IPAG and of the CDS astronomical databases SIMBAD and VIZIER.[14] This research has made use of the Washington Double Star Catalog, maintained at the U.S. Naval Observatory. We thank Nicholas Elias II for discussions. We thank Dimitri Pourbaix for maintaining and providing access to the SB9 database of RV measurements of spectroscopic binaries.

Software: MIRC pipeline (Monnier et al. 2007; Zhao et al. 2009; Che et al. 2011; Monnier et al. 2012), FIEStool (http://www.not.iac.es/instruments/fies/fiestool/), MACIM (Ireland et al. 2006), OYSTER (http://www.eso.org/~chummel/oyster/oyster.html), Wilson–Devinney code (Wilson & Devinney 1971; Wilson 1990; Wilson & Van Hamme 2014), TRICOR (Zucker et al. 1995), SPECTRUM (Gray & Corbally 1994), ELC (Orosz & Hauschildt 2000).

References

Aarum Ulvås, V., & Engvold, O. 2003a, A&A, 402, 1043
Aarum Ulvås, V., & Engvold, O. 2003b, A&A, 399, L11
Aarum Ulvås, V., & Henry, G. W. 2003, A&A, 402, 1033
Aarum, V., Berdyugina, S. V., & Ilyin, I. V. 1999, in Astrophysics with the NOT, ed. H. Karttunen & V. Piirola, 222
Bonneau, D., Clausse, J.-M., Delfosse, X., et al. 2006, A&A, 456, 789
Carlos, R. C., & Popper, D. M. 1971, PASP, 83, 504
Challouf, M., Nardetto, N., Mourard, D., et al. 2014, A&A, 570, A104
Che, X., Monnier, J. D., Zhao, M., et al. 2011, ApJ, 732, 68
Choi, J., Dotter, A., Conroy, C., et al. 2016, ApJ, 823, 102
Ducati, J. R. 2002, yCat, 2237, 0
Duemmler, R., & Aarum, V. 2001, A&A, 370, 974
Elias, N. M., II, Quirrenbach, A., Witzel, A., et al. 1995, ApJ, 439, 983
ESA (ed.) 1997, in ESA Special Publication 1200, The HIPPARCOS and TYCHO Catalogues. Astrometric and Photometric Star Catalogues Derived from the ESA HIPPARCOS Space Astrometry Mission (Noordwijk: ESA)
Flower, P. J. 1996, ApJ, 469, 355
Franciosini, E., & Chiuderi Drago, F. 1995, A&A, 297, 535
Geller, A. M., Leiner, E. M., Bellini, A., et al. 2017, arXiv:1703.10167
Glazunova, L. V., Yushchenko, A. V., Tsymbal, V. V., et al. 2008, AJ, 136, 1736
Gray, R. O., & Corbally, C. J. 1994, AJ, 107, 742
Gu, S., Tan, H., & Shan, H. 2005, ESASP, 560, 599
Gu, S., Tan, H., Wang, X., & Shan, H. 2004, in IAU Symp. 219, Stars as Suns: Activity, Evolution and Planets, ed. A. K. Dupree & A. O. Benz (San Francisco, CA: ASP), 873
Hall, D. S. 1976, in IAU Coll. 29: Multiple Periodic Variable Stars, Astrophysics and Space Science Library, Vol. 60, ed. W. S. Fitch (Dordrecht: Reidel), 287
Hauschildt, P. H., Allard, F., & Baron, E. 1999, ApJ, 512, 377
Henry, G. W., & Hall, D. S. 1997, IBVS, 4512, 1
Horch, E. P., Bahi, L. A. P., Gaulin, J. R., et al. 2012, AJ, 143, 10
Ireland, M. J., Monnier, J. D., & Thureau, N. 2006, Proc. SPIE, 6268, 62681T
Kurucz, R. 1993, ATLAS9 Stellar Atmosphere Programs and 2 km/s Grid. Kurucz CD-ROM No. 13. (Cambridge, MA: Smithsonian Astrophysical Observatory)
Leiner, E., Mathieu, R. D., & Geller, A. M. 2017, arXiv:1703.10181
Lucy, L. B. 1967, ZAp, 65, 89
Massarotti, A., Latham, D. W., Stefanik, R. P., & Fogel, J. 2008, AJ, 135, 209
McAlister, H. A., Hartkopf, W. I., Hutter, D. J., & Franz, O. G. 1987, AJ, 93, 688
Monnier, J. D., Berger, J.-P., Millan-Gabet, R., & ten Brummelaar, T. A. 2004, Proc. SPIE, 5491, 1370
Monnier, J. D., Che, X., Zhao, M., et al. 2012, ApJL, 761, L3
Monnier, J. D., Zhao, M., Pedretti, E., et al. 2007, Sci, 317, 342
Montesinos, B., Gimenez, A., & Fernandez-Figueroa, M. J. 1988, MNRAS, 232, 361
Orosz, J. A., & Hauschildt, P. H. 2000, A&A, 364, 265
Peterson, W. M., Mutel, R. L., Lestrade, J.-F., Güdel, M., & Goss, W. M. 2011, ApJ, 737, 104
Popper, D. M. 1956, ApJ, 123, 377
Roettenbacher, R. M., Monnier, J. D., Fekel, F. C., et al. 2015a, ApJ, 809, 159
Roettenbacher, R. M., Monnier, J. D., Henry, G. W., et al. 2015b, ApJ, 807, 23
Somers, G., & Pinsonneault, M. H. 2015, ApJ, 807, 174
Telting, J. H., Avila, G., Buchhave, L., et al. 2014, AN, 335, 41
ten Brummelaar, T. A., McAlister, H. A., Ridgway, S. T., et al. 2005, ApJ, 628, 453
Torres, G. 2010, AJ, 140, 1158
Torres, G., Andersen, J., & Giménez, A. 2010, A&ARv, 18, 67
Tsuru, T., Makishima, K., Ohashi, T., et al. 1989, PASJ, 41, 679
van Hamme, W. 1993, AJ, 106, 2096
van Leeuwen, F. 2007, A&A, 474, 653
Vogt, S. S., & Hatzes, A. P. 1991, in IAU Coll. 130: The Sun and Cool Stars. Activity, Magnetism, Dynamos, Vol. 380, ed. I. Tuominen, D. Moss, & G. Rüdiger (Berlin: Springer), 297
Wilson, R. E. 1990, ApJ, 356, 613
Wilson, R. E., & Devinney, E. J. 1971, ApJ, 166, 605
Wilson, R. E., & Sofia, S. 1976, ApJ, 203, 182
Wilson, R. E., & Van Hamme, W. 2014, ApJ, 780, 151
Zhao, M., Monnier, J. D., Pedretti, E., et al. 2009, ApJ, 701, 209
Zucker, S., & Mazeh, T. 1994, ApJ, 420, 806
Zucker, S., Torres, G., & Mazeh, T. 1995, ApJ, 452, 863

[13] Available at http://www.jmmc.fr/searchcal.
[14] Available at http://cdsweb.u-strasbg.fr/.